An Efficient Preprocessing Approach for Airborne Hybrid SAR and ISAR Imaging of Ship Target Based on Kernel Distribution

Rui Cao, *Graduate Student Member, IEEE*, Yong Wang, *Senior Member, IEEE*, Yanchao Lin, and Yun Zhang, *Member, IEEE*

***Abstract*— The airborne hybrid synthetic aperture radar (SAR) and inverse synthetic aperture radar (ISAR) imaging for the ship target is very important in the field of ocean surveillance, but it suffers from the problem of high computational complexity. In this article, an efficient preprocessing approach for the airborne hybrid SAR and ISAR imaging based on the kernel distribution is proposed, which can reduce the computational complexity and preserve the image quality simultaneously. First, the residual Doppler frequency is estimated. Then, a novel measurement method with good robustness is proposed for evaluating the stationarity of Doppler frequency from the aspect of statistics, which adopts the kernel distribution to estimate the probability distribution function curve for the Doppler frequency. Afterward, an effective preprocessing approach is addressed consequently to eliminate the incomplete illumination time and select the time interval with steady target motion. Results of simulated and actual SAR data verify the effectiveness of the novel algorithm proposed in this article.**

***Index Terms*—Airborne synthetic aperture radar (SAR), hybrid SAR and inverse synthetic aperture radar (ISAR) imaging, kernel distribution, preprocessing, ship target.**

NOMENCLATURE

SAR	Synthetic aperture radar.
ISAR	Inverse synthetic aperture radar.
PDF	Probability distribution function.
CS	Chirp scaling.
RD	Range-Doppler.
RID	Range-instantaneous Doppler.
$\mathrm{O}{-}\mathrm{X_e Y_e Z}$	Coordinate system of imaging scene.
$\mathrm{O}-\mathrm{XYZ}$	Coordinate system of ship target.
AMISE	Asymptotic mean integral squared error.
$\mathrm{X_p}$	Position of scatterer P in $\mathrm{O}-\mathrm{XYZ}$.
$\mathrm{X_e^P}$	Position of scatterer P in $\mathrm{O}{-}\mathrm{X_e Y_e Z}$.
θ_0	Angle between ship's bow and axis X_e.
$R_T(\theta_0)$	Transform matrix from $O-XYZ$ to $\mathrm{O}{-}\mathrm{X_e Y_e Z}$.
v_r	Velocity of aircraft.
X_e^r	Position of radar in $O-X_eY_eZ$.
t_m	Slow time.
H	Height of aircraft.
γ_0	Look angle of radar.
$\tilde{t}_m^p$	Slow time, $\tilde{t}_m^p = t_m - x_e^p/v_r$.
$R_p^S(\tilde{t}_m^p)$	Range between radar and stationary scatterer P.
R_{p0}	The shortest range in the history of $R_p^S(\tilde{t}_m^p)$.
$f_d^S(\tilde{t}_m^p)$	Doppler frequency of SAR platform.
$\varphi_s(\tilde{t}_m^p)$	Squint angle.
$f_d(\tilde{t}_m^p)$	Doppler frequency of echo data.
$f_d^I(\tilde{t}_m^p)$	Doppler frequency of ISAR imaging target.
$\hat{f}_d^I(\tilde{t}_m^p)$	Estimated values of $f_d^I(\tilde{t}_m^p)$.
$\overline{f_d^I}$	Mean value of $f_d^I(\tilde{t}_m^p)$.
t_r	Fast time.
$a_r(\cdot)$	Amplitude function of range direction.
$a_a(\cdot)$	Amplitude function of azimuth direction.
K_r	Frequency modulation radio.
$s_m(t_r)$	Matching function.
$s_{rb}(t_m, t_r)$	Echo data after range compensation.
$\mathrm{FFT}[\cdot]$	FFT operator.
$\mathrm{IFFT}[\cdot]$	IFFT operator.
m_{ns}	Start pulse order of range profile.
$s_{rb}(m, n)$	Discrete form of $s_{rb}(t_r, t_m)$.
$\mathbf{s_{rb}^k}(n)$	The kth subdata.
k	Order of subdata, $k = 1, 2, \ldots, K$.
K	Number of subdata, $K = \lfloor N_a/N_{a0} \rfloor$.
N_a	Pulse number of range profile.
N_{a0}	Pulse number of subdata.
$s(m_1, n)$	Result of conjugated multiplication.
m_1	Azimuth order of $s(m_1, n)$, $m_1 = 1, 2, \ldots, N_{a0} - 1$.
$R_0(n)$	Correlation function of $s(m_1, n)$.
R_b	Autocorrelation function of $R_0(n)$.
f_{dc}^k	Doppler frequency center of subdata.
PRT	Pulse repetition time.
$\mathrm{angle}(\cdot)$	Operator of extracting phase.
$\hat{f}_d(k)$	Estimated values of echo data, $\hat{f}_d(k) = \{f_{\mathrm{dc}}^k\}$.
$f_d^S(k)$	Discrete from of $f_d^S(\tilde{t}_m^p)$.

Manuscript received January 24, 2022; revised April 3, 2022 and May 12, 2022; accepted June 10, 2022. Date of publication June 15, 2022; date of current version July 4, 2022. This work was supported in part by the National Natural Science Foundation of China under Grant 61871146, and in part by the Fundamental Research Funds for the Central Universities under Grant FRFCU5710093720. *(Corresponding author: Yong Wang.)*

Rui Cao, Yong Wang, and Yun Zhang are with the Research Institute of Electronic Engineering Technology, Harbin Institute of Technology, Harbin 150001, China (e-mail: caor@hit.edu.cn; wangyong6012@hit.edu.cn; zhangyunhit@hit.edu.cn).

Yanchao Lin is with the National Key Laboratory of Science and Technology on Aerospace Intelligent Control, Beijing Aerospace Automatic Control Institute, Beijing 100854, China (e-mail: linyanchao110@qq.com).

Digital Object Identifier 10.1109/JSTARS.2022.3183196

$\hat{f}_d^I(k)$	Discrete form of $\hat{f}_d^I(\tilde{t}_m^p)$.
δ_{opt}	Optimal bandwidth.
f_p	Optimal central frequency.
p_i	Polynomial coefficient.
n_p	Polynomial order.
m_s	Optimal start time of echo data.
m_e	Optimal end time of echo data.
$\mathbf{s_r^{opt}}(n)$	Echo data with optimal time.
$f_\delta(x)$	Estimated PDF of $\hat{f}_d^I(k)$.
$N(\cdot)$	Normal distribution function.

I. Introduction

AIRBORNE synthetic aperture radar (SAR) imaging of ship target plays a significant role in the field of marine monitoring [1]–[3]. Due to the complex motion of ship target, the traditional SAR imaging algorithm will generate a defocused radar image. To produce a well-focused radar image, the hybrid SAR and inverse synthetic aperture radar (ISAR) technique is presented, which can process the motion of radar and target separately [4]–[10]. The idea of hybrid SAR and ISAR imaging was originally proposed and verified via simulated experiment by Ward [11]–[12]. Afterward, Martorella *et al.* presented a series of hybrid SAR and ISAR imaging algorithms combining with the techniques of Doppler parameter estimation, cross-range scaling, and moving target detection [13]–[16]. Moreover, F. Breizzi proposed an autofocusing algorithm for hybrid SAR and ISAR imaging in [17]. Some constructive conclusions have been obtained for these algorithms. A hybrid imaging algorithm for high-squint SAR was proposed in [18], which focused on the modification of SAR compensation process. In [19], a hybrid imaging algorithm based on the CLEAN technique and cross-range scaling for frequency-modulated continuous-wave SAR was presented by E. Casalini *et al.*, which verified the possibility of radar imaging for the frequency modulation continuous wave in the Ka band. Recently, a novel time-frequency analysis technique is addressed in [20], which can be applied in the range-instantaneous Doppler (RID) analysis for the high-resolution imaging. For the high sea condition, the ISAR imaging technique in [21] can achieve the excellent performance, in which a high accuracy parameter estimation method was presented.

Whereas, some of these hybrid SAR and ISAR imaging methods have the disadvantages as follows:

1) High computational complexity: The hybrid SAR and ISAR imaging methods proposed in [10]–[19] suffer from the high computational complexity owing to processing the entire echo data. Some imaging time selection methods are proposed in [22]–[28], in which the Doppler frequency is segmented in time, and the stationarity is evaluated by the indexes such as image contrast [22] and root mean square error [27]. Hence, the selected time window will be affected by the segment length. Moreover, these methods determine the time window during the ISAR imaging, before which the high computational complexity has been produced. Given the above, the optimal processing time should be determined during the SAR processing, which is denoted as the preprocessing approach for the hybrid SAR and ISAR imaging in this article.

2) Influence on the quality of ship radar image: The performance of hybrid SAR and ISAR algorithm is influenced by the long period movement of ship target. Hence, the optimal time interval selection is necessary for enhancing the image quality.

In this article, the computational complexity can be reduced from two aspects, including the determination of optimal time during the SAR processing and the removal of the incomplete illumination time. For the former, the computational complexity will be greatly degraded owing to processing the data with small size in the ISAR processing. For the latter, the ship target is illuminated in a limited time that can be composed of the incomplete illumination time and the complete illumination time, respectively. Here, the complete illumination time is defined as the time interval in which the entire ship target is located in the wave beam. Correspondingly, the incomplete illumination time is defined as the time interval in which the ship target is partially illuminated by the wave beam. Obviously, the radar image with the entire ship target cannot be obtained via the incomplete illumination time, which will also induce the additional computing time. Hence, the more computational complexity can be reduced via selecting the complete illumination time and ignoring the incomplete illumination time.

For this purpose, an efficient preprocessing approach is proposed in this article for the airborne hybrid SAR and ISAR imaging based on the kernel distribution. First, the Doppler frequencies of echo data are estimated via the average cross-correlation coefficient (ACCC) method in [29]. Then, a novel estimation method for the residual Doppler frequency is proposed. The residual Doppler frequency can reflect the illuminated scope and movement of the imaging target. Afterwards, an efficient preprocessing approach is proposed, through which the optimal processing time interval can be selected. For determining the optimal time interval, the stationarity of residual Doppler frequency needs to be measured. In this article, the kernel distribution in [29] is adopted to estimate the probability distribution function (PDF) of residual Doppler frequency and generate a central frequency and bandwidth, through which the optimal time interval can be determined.

The proposed approach has the advantages as follows. First, it can degrade the computational complexity via determining the optimal time interval during the SAR processing. Second, the stationarity of Doppler frequency is measured from the aspect of statistics, which is accurate and efficient compared with the existing methods in [23]–[28]. Third, the image quality can be equal or higher compared with the radar image before the SAR procedure.

The main work of this article is shown in Fig. 1. The main contents are arranged as follows. First, the circumstances of stationary and moving ship target are analyzed in Section II. Then, an efficient preprocessing approach is proposed in Section III, including the residual Doppler frequency estimation and the optimal time interval selection. Afterwards, the results of

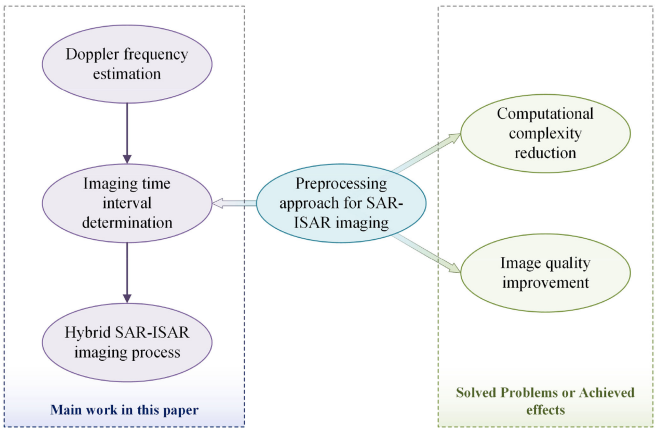

Fig. 1. Main work of this article.

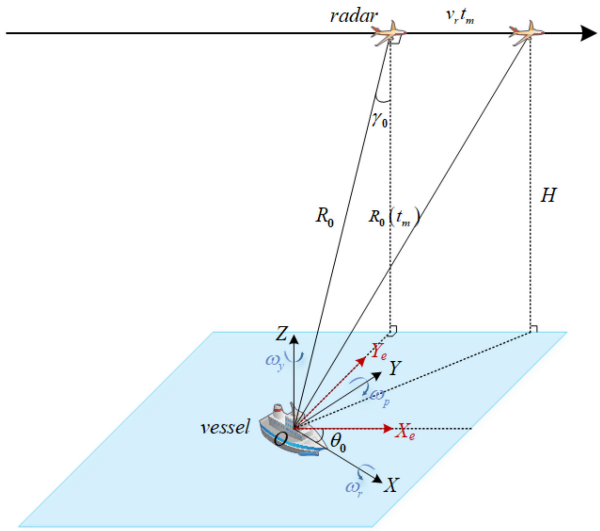

Fig. 2. Airborne SAR imaging geometry.

simulated and actual SAR data are shown in Section IV. Finally, the conclusion is drawn in Section V.

II. Hybrid SAR and ISAR Imaging Geometry Model

The circumstances of stationary ship target and moving ship target are discussed in this section. First, the SAR imaging geometry model is established. On this basis, the range history and Doppler frequency produced by the SAR platform are deduced. Second, the hybrid SAR and ISAR imaging geometry is analyzed. Consequently, the range history and Doppler frequency generated by the SAR platform and ISAR imaging target are derived.

A. Circumstance of Stationary Ship Target

The airborne SAR imaging geometry is shown in Fig. 2, in which the imaging scene and target coordinate systems are established, which are denoted as $\mathrm{O}-\mathrm{X_eY_eZ}$ and $\mathrm{O}-\mathrm{XYZ}$, respectively. The scene center is denoted as O, the direction of ship's bow is the same as axis X, and the axis Z is vertical to the sea surface.

For simplification, we choose the ship target with the center located at O for the following analysis. When the ship target is stationary, the positions of scatterer P on the ship target in the coordinates of $\mathrm{O}-\mathrm{XYZ}$ and $\mathrm{O}-\mathrm{X_eY_eZ}$ can be expressed as follows:

$$\mathbf{X_p} = [x_p, y_p, z_p]^{\mathrm{T}} \tag{1}$$

$$\begin{aligned}\mathbf{X_e^P} &= [x_e^p, y_e^p, z_p]^{\mathrm{T}} \\ &= \mathbf{R_T}(\theta_0)\,\mathbf{X_p} \\ &= [x_p\cos\theta_0 + y_p\sin\theta_0, -x_p\sin\theta_0 + y_p\cos\theta_0, z_p]^{\mathrm{T}}\end{aligned} \tag{2}$$

where θ_0 is the angle between the ship's bow and axis $\mathrm{X_e}$ and $\mathbf{R_T}(\theta_0)$ is the transform matrix from the coordinate of $\mathrm{O}-\mathrm{XYZ}$ into $\mathrm{O}-\mathrm{X_eY_eZ}$, and it can be expressed as

$$\mathbf{R_T}(\theta_0) = \begin{bmatrix} \cos\theta_0 & \sin\theta_0 & 0 \\ -\sin\theta_0 & \cos\theta_0 & 0 \\ 0 & 0 & 1 \end{bmatrix}. \tag{3}$$

The aircraft is moving along the direction of axis $\mathrm{X_e}$with a velocity of v_r. The position of radar in the coordinate of $\mathrm{O}-\mathrm{X_eY_eZ}$ is shown as

$$\mathbf{X_e^r}(t_m) = [v_r t_m, H\tan\gamma_0, H]^{\mathrm{T}} \tag{4}$$

where t_m, H, and γ_0 are the slow time, the flight height of aircraft, and the look angle of radar, respectively.

The range between the radar and scatterer P is calculated as

$$\begin{aligned}R_p^S(t_m) &= \|\mathbf{X_e^r}(t_m) - \mathbf{X_e^P}\|_2 \\ &= \left[R_{p0}^2 + (v_r t_m - x_e^p)^2\right]^{\frac{1}{2}}\end{aligned} \tag{5}$$

where the range R_{p0} can be expressed as

$$R_{p0} = \left[(H\tan\gamma_0 - y_e^p)^2 + (H - z_p)^2\right]^{\frac{1}{2}}. \tag{6}$$

Then, the range history can be rewritten as

$$R_p^S(\tilde{t}_m^p) = \left[R_{p0}^2 + (v_r\tilde{t}_m^p)^2\right]^{\frac{1}{2}} \tag{7}$$

where $\tilde{t}_m^p = t_m - x_e^p/v_r$. The relationship between R_{p0} and $R_p^S(\tilde{t}_m^p)$ is shown in Fig. 3.

Afterwards, taking the derivative of $R_p(\tilde{t}_m^p)$, the Doppler frequency produced by the SAR platform can be calculated as

$$f_d^S(\tilde{t}_m^p) = \frac{2v_r\cos\varphi_s(\tilde{t}_m^p)}{\lambda} \tag{8}$$

where $\varphi_s(\tilde{t}_m^p)$ is the angle between the direction of axis X and the RLOS in Fig. 3. The squint angle $\varphi_s(\tilde{t}_m^p)$ can be expressed as

$$\varphi_s(\tilde{t}_m^p) = \begin{cases} \arctan\left(-\frac{R_{p0}}{v_r\tilde{t}_m^p}\right), & \tilde{t}_m^p \le 0 \\ \pi - \arctan\left(\frac{R_{p0}}{v_r\tilde{t}_m^p}\right), & \tilde{t}_m^p > 0. \end{cases} \tag{9}$$

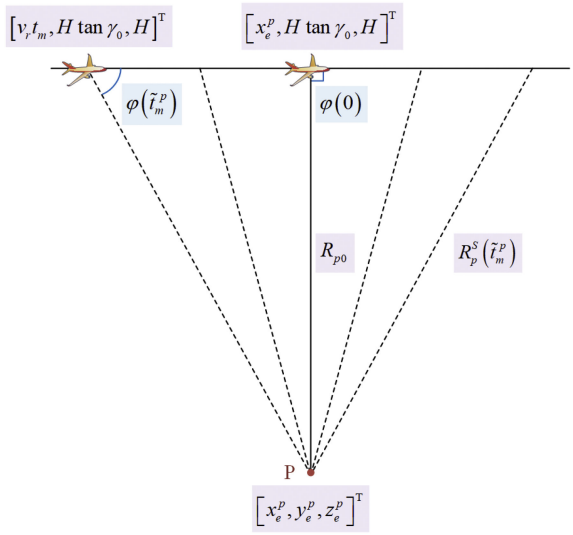

Fig. 3. Relationship between range R_{p0} and $R_p^S(\tilde{t}_m^p)$.

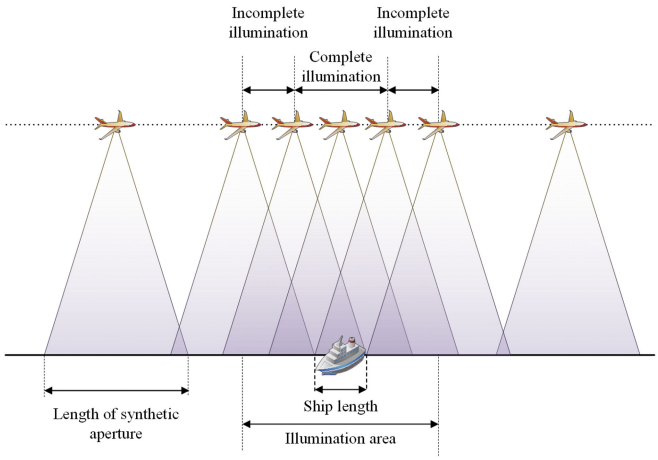

Fig. 4. Illumination area of ship target.

B. Circumstance of Moving Ship Target

The ship target on the sea surface has the three-dimensional (3-D) rotation and translational motion. Under this circumstance, the position of scatterer P in the coordinates of $\mathrm{O}-\mathrm{XYZ}$ and $\mathrm{O}-\mathrm{X_eY_eZ}$ can be calculated as follows:

$$\begin{aligned}\mathbf{X_p}(t_m) &= [x_p(t_m), y_p(t_m), z_p(t_m)]^{\mathrm{T}} \\ &= \mathbf{R_{rot}}(t_m)\mathbf{X_p} + [v_t t_m, 0, 0]^{\mathrm{T}} \qquad (10)\\ \mathbf{X_e^p}(t_m) &= [x_e^p(t_m), y_e^p(t_m), z_e^p(t_m)]^{\mathrm{T}} \\ &= \mathbf{R_T}(\theta_0)\mathbf{X_p}(t_m) \qquad (11)\end{aligned}$$

where v_t is the forward velocity of ship and $\mathbf{R_{rot}}(t_m)$ represents the 3-D rotation matrix.

Then, the range between scatterer P and radar can be calculated as

$$R_p(\tilde{t}_m^p) = \left[R_{p0}^2(\tilde{t}_m^p) + (v_r\tilde{t}_m^p)^2\right]^{\frac{1}{2}} \qquad (12)$$

where the range $R_{p0}(\tilde{t}_m)$ can be expressed as

$$\begin{aligned}R_{p0}(\tilde{t}_m^p) &= \left[(H\tan\gamma_0 - y_e^p(t_m))^2 + (H - z_p(t_m))^2\right]^{\frac{1}{2}} \\ &= R_{p0} + \triangle R_{p0}(\tilde{t}_m^p). \qquad (13)\end{aligned}$$

The range variation produced via the target motion is denoted as $\triangle R_{p0}(\tilde{t}_m^p)$. Since the position variation of ship target is not large, the time variable $\tilde{t}_m^p = t_m - x_e^p(t_m)/v_r$ can be approximated as $\tilde{t}_m^p \approx t_m - x_e^p/v_r$.

Furthermore, by taking the derivative of $R_p(\tilde{t}_m^p)$, the Doppler frequency can be computed as

$$f_d(\tilde{t}_m^p) = f_d^S(\tilde{t}_m^p) + f_d^I(\tilde{t}_m^p) \qquad (14)$$

where $f_d(\tilde{t}_m^p)$ is the Doppler frequency generated by the hybrid SAR and ISAR imaging target, $f_d^I(\tilde{t}_m^p)$ is the Doppler frequency produced via the ISAR imaging target, and the expression of $f_d^I(\tilde{t}_m^p)$ is $-2\triangle\dot{R}_{p0}(\tilde{t}_m^p)/\lambda$.

Hence, the Doppler frequency can be decomposed into the combination of frequency produced by the SAR and ISAR procedure.

III. Preprocessing Approach Based on Kernel Distribution

In this section, an efficient preprocessing approach is proposed for the airborne hybrid SAR and ISAR imaging based on the kernel distribution. First, the principle of preprocessing approach is elaborated via the analysis of Doppler frequency. Second, the proposed preprocessing approach is introduced, in which the residual Doppler frequency is estimated, and the stationarity is measured with the method in statistics. On this basis, the optimal processing time interval can be determined.

A. Principle of Preprocessing Approach

Actually, the ship target is illuminated by the wave beam only in a limited time. The length of synthetic aperture is larger than the size of ship target, and the illuminated time consists of the complete and incomplete illumination time. Hence, the computational complexity can be reduced via ignoring the incomplete illumination time.

Furthermore, both the smooth motion and maneuvering movement exist in the complete illumination time. The smooth motion will produce the steady Doppler frequency and has little impact on the radar image quality. Whereas, the maneuvering movement will generate the time-varying Doppler frequency and decrease the image quality. Therefore, the image quality can be enhanced via ignoring the time interval with maneuvering motion of target.

Via the analysis above, we can see that the status of illumination and target motion can be reflected in the residual Doppler frequency, which is related to the theoretical Doppler frequency value of SAR platform and the Doppler frequency center of echo. The theoretical Doppler frequency value, Doppler frequency of echo, and residual Doppler frequency can be calculated as follows.

First, the theoretical Doppler frequency value of SAR platform can be calculated by (8).

Second, the Doppler frequency center of echo can be estimated via the ACCC method in [29]. The ACCC method utilizes the correlation of adjacent echoes to estimate the Doppler frequency center [29]. When the target is not completely illuminated, the correlation of adjacent echoes will be degraded, which induces the obvious difference between the estimated value and theoretical value. As seen in (14), the Doppler frequency is generated by the SAR platform and the ISAR imaging target. When the target has maneuvering motion, the Doppler frequency of ISAR imaging target will be large, which will also cause the obvious difference between the estimated value and theoretical value. Here, this difference can be denoted as the residual Doppler frequency.

Third, the residual Doppler frequency can be estimated as

$$\hat{f}_d^I\left(\tilde{t}_m^p\right) = \hat{f}_d\left(\tilde{t}_m^p\right) - f_d^S\left(\tilde{t}_m^p\right). \tag{15}$$

To avoid the influence produced by the translational motion of ship target, the residual Doppler frequency in (15) can be calculated as follows:

$$\overline{f_d^I} = E\left[\hat{f}_d^I\left(\tilde{t}_m^p\right)\right] \tag{16}$$

$$\hat{f}_d^I\left(\tilde{t}_m^p\right) = \hat{f}_d^I\left(\tilde{t}_m^p\right) - \overline{f_d^I}. \tag{17}$$

The residual Doppler frequency in (17) can reflect the status of illumination and target motion, by which the optimal time interval can be determined. When the target has the smooth movement in the complete illumination time, the residual Doppler frequency is stable, and it is concentrated on a stationary frequency. Otherwise, the residual Doppler frequencies is time-varying and dispersive.

The proposed calculation method of residual Doppler frequency is different from the other optimal time selection methods, such as [23]–[27]. In the existing methods, the residual Doppler frequency is calculated with the SAR processing, motion compensation, ISAR refocusing, and time-frequency analysis for the echo data with entire pulses. Hence, the calculation of the residual Doppler frequency consumes a heavy computational complexity.

The proposed method can calculate the residual Doppler frequency only with the range compensation and ACCC method in [29], which reduces the computational complexity.

Moreover, the proposed method is easy to implement compared with other optimal time selection methods. In the existing methods, the time-frequency analysis technique is applied to estimate the residual Doppler frequency, and the range bin with the single scatterer is usually required consequently, which does not exist in some actual cases. Although several time-frequency curve extraction methods are proposed in [23]–[27], the processing procedure becomes complicated and the more computational complexity is produced.

The proposed method can accomplish the calculation of the residual Doppler frequency without finding the range bin with the single scatterer or extracting the time-frequency curve of the single scatterer. The procedure of the proposed method can be implemented easily only with the range compensation and ACCC method.

B. Preprocessing Approach Based on Kernel Distribution

As mentioned above, the stationarity of residual Doppler frequency is related to the computational complexity and image quality. In this article, the kernel distribution in the statistics is applied to evaluate the stationarity of residual Doppler frequency. The stationarity of Doppler frequency is depicted as a central frequency and a narrow bandwidth. On this basis, an efficient preprocessing approach is proposed for determining the optimal time interval, which can reduce the computational complexity and ensure the image quality.

The main procedures of the proposed preprocessing approach are illustrated as follows:

Step (1): Obtain the range compression result for the echo data.

The range profile can be obtained via the matched filtering approach. The echo signal of scatterer P can be represented as

$$s_r\left(t_m, t_r\right) = a_r\left(t_r - \frac{2R_p\left(t_m\right)}{c}\right) a_a\left(t_m\right) \cdot \exp\left[j\pi K_r\left(t_r - \frac{2R_p\left(t_m\right)}{c}\right)^2 - j\frac{4\pi}{\lambda}R_p\left(t_m\right)\right] \tag{18}$$

where t_r is the fast time, $a_r(\cdot)$ and $a_a(\cdot)$ are the amplitude functions of range and azimuth direction, and K_r is the frequency modulation ratio.

The matching function is

$$s_m\left(t_r\right) = a_r\left(t_r\right)\exp\left(-j\pi K_r t_r^2\right). \tag{19}$$

Then, the echo data after range compression can be obtained as

$$s_{rb}\left(t_m, t_r\right) = \mathrm{IFFT}\left[\mathrm{FFT}_{t_r}\left[s_r\left(t_m, t_r\right)\right]\mathrm{FFT}_{t_r}\left[s_m\left(t_r\right)\right]\right] \tag{20}$$

where $\mathrm{FFT}[\cdot]$ and $\mathrm{IFFT}[\cdot]$ are the fast Fourier transform (FFT) and inverse FFT (IFFT) operator, respectively.

Step (2): Extract the range profile and divide it into subdata.

The range profile of one ship target is extracted. The start pulse order of this range profile is denoted as m_{ns}. The discrete form of this range profile is represented as $s_{rb}(m, n)$, where m and n are the azimuth and range order, respectively. Then, the range profile is divided into some subdata with the form of

$$\mathbf{s_{rb}^k}\left(n\right) = \begin{bmatrix} s_{rb}\big(\left(k-1\right)N_{a0} + m_{n_s}, n\big) \\ s_{rb}\big(\left(k-1\right)N_{a0} + m_{n_s} + 1, n\big) \\ \vdots \\ s_{rb}\big(\left(k-1\right)N_{a0} + m_{n_s} + N_{a0} - 1, n\big) \end{bmatrix} \tag{21}$$

where $k = 1, 2, \ldots, K$ is the order of subdata, $K = \lfloor N_a/N_{a0} \rfloor$ is the number of subdata, and N_a and N_{a0} are the pulse number of range profile and subdata, respectively.

Step (3): Estimate the Doppler frequency of echo data based on the ACCC method in [29].

The main procedures of Doppler frequency center estimation method are as follows:

1) The matrix $s(m_1, n)$ is obtained by the conjugated multiplication of two neighboring pules, which can be expressed as

$$s\left(m_1, n\right) = \left[s_{rb}^{k}\left(m_1, n\right)\right]^{*} s_{rb}^{k}\left(m_1 + 1, n\right) \tag{22}$$

where $m_1 = 1, 2, \ldots, N_{a0} - 1$ is the azimuth order of $s(m_1, n)$.

2) The correlation function $R_0(n)$ is generated by calculating the average along the azimuth direction, which can be represented as

$$R_0\left(n\right) = \frac{1}{N_{a0} - 1} \sum_{m_1=1}^{N_{a0}-1} s\left(m_1, n\right). \tag{23}$$

3) The autocorrelation function R_b is computed by calculating the average along the range direction, which can be expressed as

$$R_b = \frac{1}{N_r} \sum_{n=1}^{N_r} R_0\left(n\right). \tag{24}$$

4) The Doppler frequency center can be estimated as

$$f_{dc}^{k} = \frac{\text{angle}\left(R_b\right)}{2\pi \cdot \text{PRT}} \tag{25}$$

where PRT is the pulse repetition time and $\text{angle}(\cdot)$ is the function of extracting phase.

5) The Doppler frequency history of echo data can be generated as

$$\hat{f}_d\left(k\right) = f_{dc}^{k} \quad , k = 1, 2, \ldots, K. \tag{26}$$

Step (4): Calculate the Doppler frequency of SAR platform with (8), and it is denoted as $f_d^S(k)$.

Step (5): Estimate the residual Doppler frequency with (15)–(17), and the Doppler frequency of ISAR imaging target is denoted as $\hat{f}_d^I(k)$.

Step (6): Determine the optimal central frequency of f_p and optimal bandwidth of δ_{opt}.

The optimal central frequency and bandwidth determination approach based on the kernel distribution will be elaborated in Section III-C.

Step (7): Obtain the time interval based on f_p and δ_{opt}.

The residual Doppler frequency is selected by the central frequency f_p and bandwidth δ_{opt}, i.e., $|\hat{f}_d^I(k) - f_p| \le \delta_{\text{opt}}$, which can illustrate that the ship target has the smooth motion in the complete illumination time. For better determining the imaging time interval, the Doppler frequency $\hat{f}_d^I(k)$ can be fitted by the polynomial, which can be expressed as

$$\hat{f}_d^I\left(m\right) = \sum_{i=0}^{n_p} p_i m^i \tag{27}$$

where p_i and n_p are the polynomial coefficient and order, respectively.

The start and end pulse order which are satisfied with $|\hat{f}_d^I(k) - f_p| \le \delta_{opt}$ are denoted as m_s and m_e, respectively. Then, the time interval can be obtained as $[m_{ns} + m_s, m_{ns} + m_e] \cdot \text{PRT}$, and the corresponding echo data

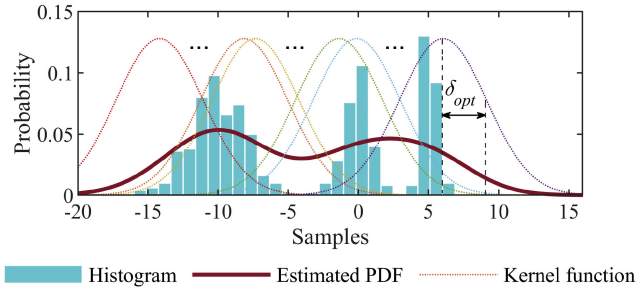

Fig. 5. Illustration diagram for the kernel distribution method.

can be expressed as

$$\mathbf{s_r^{opt}}\left(n\right) = \begin{bmatrix} s_r\left(m_{ns} + m_s, n\right) \\ s_r\left(m_{ns} + m_s + 1, n\right) \\ \vdots \\ s_r\left(m_{ns} + m_e, n\right) \end{bmatrix}. \tag{28}$$

Here, the procedure of preprocessing approach is accomplished.

Remark 1: In this article, the Doppler frequency center is estimated via (25), which is suitable for the ship ISAR imaging with high SNR [29]. Under the high sea condition, the sea clutter may exist and the SNR will be decreased. Then, the sea clutter suppression techniques in [35] and [36] can be applied, and the more precious Doppler centroid estimation method in [37] can be utilized consequently.

C. Optimal Selection Approach for the Central Frequency and Bandwidth Based on the Kernel Distribution

Since the PDF can describe the probability of appearing at each frequency, the central frequency, and optimal bandwidth in *Step (6)* can be obtained by estimating the PDF curve of the residual Doppler frequency. In this article, an optimal selection approach for the central frequency and bandwidth based on the kernel distribution is proposed.

The kernel distribution is a nonparametric method for the estimation of PDF, which describes each sample with a kernel function, and sums all the kernel functions to generate a smooth PDF curve. The principle of kernel function method is illustrated as Fig. 5. The shapes of kernel function can be normal, triangle, and box. Considering the good smoothness, the standard normal distribution is selected. Moreover, an appropriate bandwidth is important because it usually controls the smoothness of PDF curve. In this article, the bandwidth is calculated by the theory in [29].

For the estimated PDF, the position of the highest peak is denoted as f_p, which reflects that the most amount of Doppler frequencies are concentrated on f_p, and the bandwidth can describe the concentration of central frequency.

The main procedures of the proposed approach can be seen in Fig. 6, and the central frequency and optimal bandwidth can be determined as follows.

Step (1): Estimate the PDF of residual Doppler frequency via the kernel distribution.

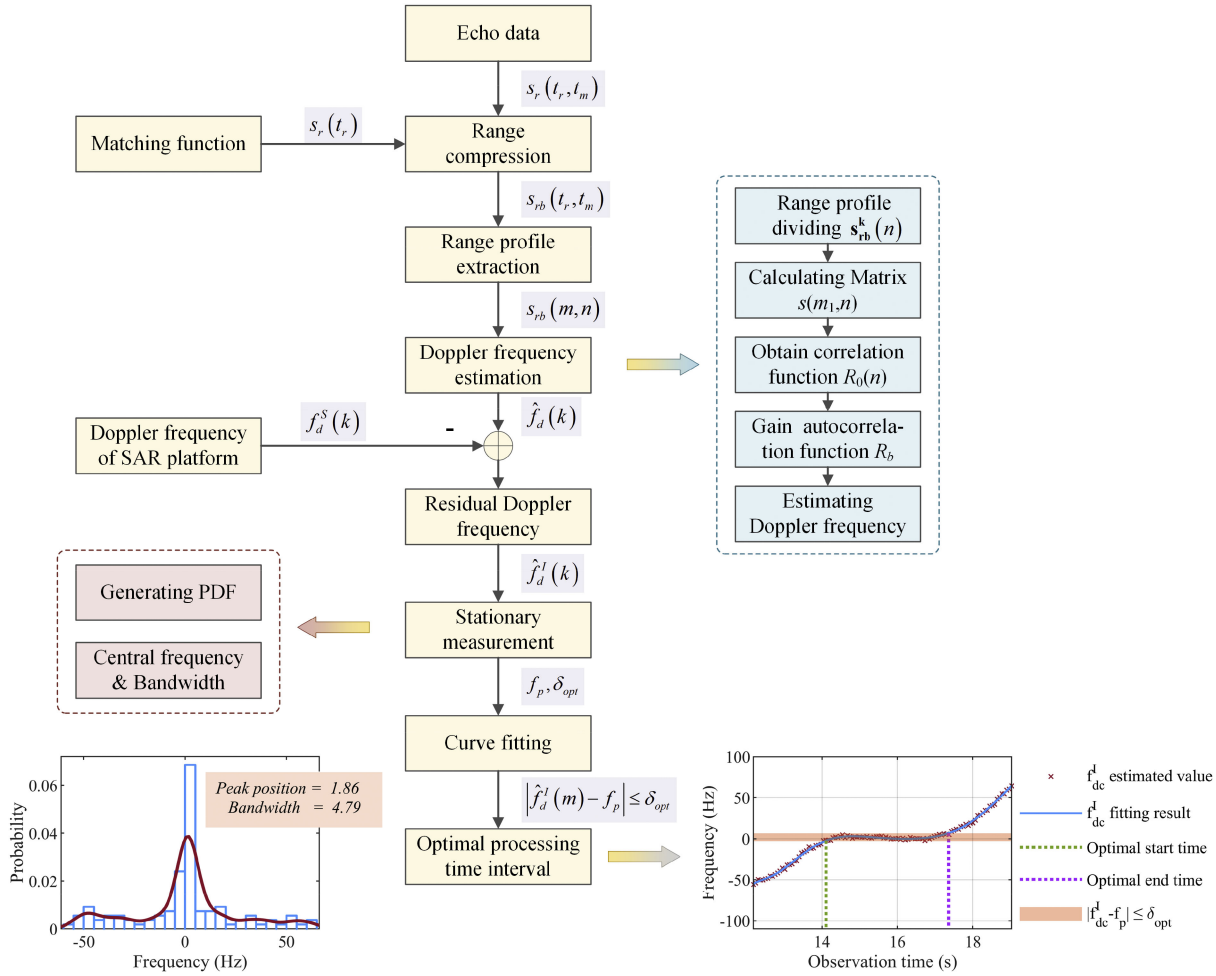

Fig. 6. Flowchart of proposed preprocessing approach based on kernel distribution.

The PDF of residual Doppler frequency is calculated via the kernel function, which can be expressed as

$$f_\delta(x) = \frac{1}{K\delta}\sum_{k=1}^{K} N\left(\frac{x-\hat{f}_d^I(k)}{\delta}\right) \tag{29}$$

where δ is the bandwidth of kernel function, x represents the real values, the kernel function we choose in this article is the standard normal distribution which has a better smoothness, $N(\cdot)$ represents the standard normal distribution, and the expression of $N(\cdot)$ is given as

$$N(x) = \frac{1}{\sqrt{2\pi}}\exp\left(-\frac{x^2}{2}\right). \tag{30}$$

Step (2): Determine the optimal central frequency and bandwidth.

The optimal central frequency can be solved by searching the highest peak position, which reflects the most amount of Doppler frequencies are concentrated on this position.

The optimal bandwidth of δ_{opt} can be calculated by the principle of minimizing the asymptotic mean integral squared error (AMISE) in [29].

The mean of $f_\delta(x)$ can be calculated by

$$\begin{aligned} E\{f_\delta(x)\} &= \int \frac{1}{\delta}N\left(\frac{x-z}{\delta}\right)f(z)\,\mathrm{d}z \\ &\approx f(x) + \frac{\delta^2}{2}\sigma^2\ddot{f}(x) \end{aligned} \tag{31}$$

where $f(\cdot)$ is the true density and z is the variable of integration.

With the Taylor expansion, the variance of $f_\delta(x)$ can be approximated as

$$\mathrm{var}\{f_\delta(x)\} \approx \frac{1}{K\delta}f(x)\int\left[\frac{1}{\delta}N\left(\frac{x-z}{\delta}\right)\right]^2\mathrm{d}z. \tag{32}$$

Then, the mean integral squared error can be calculated as

$$\mathrm{MISE}(f_\delta(x)) = E\left\{\int[f_\delta(x)-f(x)]^2\mathrm{d}x\right\}. \tag{33}$$

With the weak assumption and Taylor expansion, we can obtain the AMISE as

$$\mathrm{AMISE}(f_\delta(x)) = \frac{\delta^4}{4}\sigma^4\int\left(\ddot{f}(x)\right)^2\mathrm{d}x$$

$$+\frac{1}{K\delta}\int\left[\frac{1}{\delta}N\left(\frac{x-z}{\delta}\right)\right]^2\mathrm{d}z. \quad (34)$$

Calculating the derivation of AMISE$(f_\delta(x))$ and setting it to be equal to zero, the optimal bandwidth can be computed as

$$\delta_{opt}=\left(\frac{4\sigma^5}{3K}\right)^{\frac{1}{5}}\approx 1.06\sigma K^{-\frac{1}{5}} \quad (35)$$

where σ is the standard deviation of Doppler frequency samples.

The optimal bandwidth in (35) describes the frequency range that can be regarded as neighboring the central frequency. With the optimal central frequency and bandwidth, the residual Doppler frequency in the domain of $|\hat{f}_d^I(k)-f_p|\le\delta_{\text{opt}}$ can be considered as stable. Afterwards, the preprocessing procedure can be accomplished.

The proposed approach can maintain or enhance the image quality owing to the selection for the stable Doppler frequency, and the computational will be degraded obviously. Whereas, the azimuth resolution will be reduced due to the decrease of pulse number or imaging time.

Compared with the other optimal time selection methods, the proposed approach can reduce more computational complexity.

Reason 1: Processing the echo data with smaller size in the procedure of motion compensation and ISAR refocusing.

In the existing methods, the optimal time interval is determined after the SAR processing, motion compensation, and ISAR refocusing for the echo data with the entire pulses. Hence, a heavy computational complexity is required owing to process the echo data with the entire pulses.

In the proposed approach, the optimal time interval is determined after the range compensation of the SAR processing, and then the motion compensation and ISAR imaging are implemented for the echo data with the few pulses. Therefore, the proposed method can reduce more computational complexity in the process of motion compensation and ISAR imaging.

Reason 2: Without the generation of the image sequence.

In some existing methods, the image sequence is generated to determine the optimal time interval, which produces a large computational complexity.

In the proposed approach, the optimal time interval is selected with the stationary Doppler frequency, which is obtained based on the probability estimation. This procedure consumes a tolerable computational complexity compared with the image sequence generation in the other methods.

Moreover, the proposed approach can adapt the case of maneuvering motion of the ship target. Owing to the change of target motion, the estimated PDF curve can show the multiple peaks. For the better image quality, the higher peak can be selected to determine the optimal time interval, because the more amount of Doppler frequencies are concentrated on this peak position.

Furthermore, the proposed approach can be applied in the circumstance of high sea state. If the rotation amplitudes are different in the multiple periods, the multiple peaks will exist in the estimated PDF curve, and the Doppler frequencies are concentrated on the different frequencies. The optimal time interval can be determined by the maximum peak position and bandwidth. If the rotation amplitude is same in the multiple periods, the peak value will be larger compared with the case of single period, and more amount of Doppler frequencies are concentrated on the peak position. With the peak position and bandwidth, multiple time intervals can be determined. Considering the higher imaging resolution, the optimal time interval with the largest imaging time can be selected.

TABLE I
PARAMETERS OF THE RADAR AND IMAGING SCENE

Parameters	Values
Bandwidth	400 MHz
Sample frequency	480 MHz
Carrier frequency	5.3 GHz
Pulse width	10 μs
PRF	200 Hz
Aircraft height	6 km
Aircraft velocity	50 m/s
Scene length	800 m
Scene width	800 m

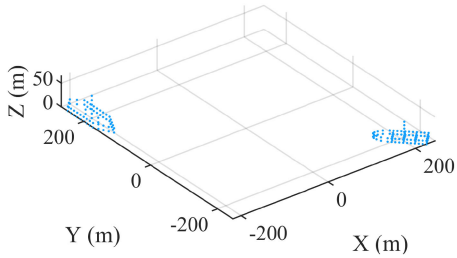

Fig. 7. Radar imaging scene and the ship's scatterer models.

IV. EXPERIMENTAL RESULT

In this section, the results of simulated and actual SAR data are given to verify the effectiveness of the proposed approach. There are multiple ship targets in the imaging scene. First, the proposed preprocessing approach is implemented to produce the optimal time interval. Afterwards, the hybrid SAR and ISAR imaging algorithm in [13] is applied to generate the well-focused ship radar image. Here, the Chirp Scaling (CS) algorithm in [31] and [32] is chosen for the SAR processing, the range alignment method in [33] and the phase compensation method in [34] are used for the motion compensation, and the RID algorithm based on the spectrum in [10] and [38] is used for the ISAR refocusing.

A. Simulated Data

First, the effectiveness of the proposed approach is verified with the results of simulated experiments. The parameters of the radar and imaging scene are listed in Table I. Two ship targets are located in the scene as shown in Fig. 7, and the 3-D rotating parameters are given in Table II according to the values in [39] and [40]. The SAR image via the CS algorithm is shown in Fig. 8. It is obvious that the CS images of two ship targets are defocused in the azimuth without the preprocessing procedure. Hence, the echo data should be preprocessed to reduce the computing time

TABLE II
ROTATION PARAMETERS OF THE SHIP TARGET

Ship target	Direction	Amplitude (°)	Angle velocity (°/s)
1	Roll	5.00	26.4
	Pitch	0.90	11.2
	Yaw	1.33	13.0
2	Roll	7.20	12.2
	Pitch	0.85	6.7
	Yaw	0.95	14.2

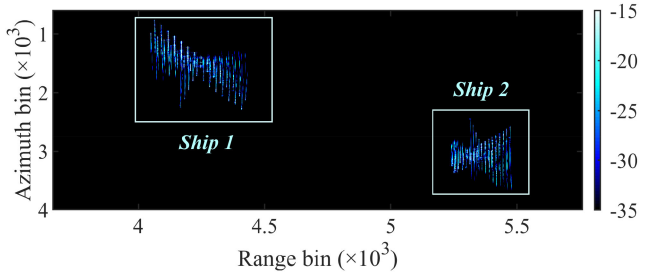

Fig. 8. SAR imaging results with CS algorithm.

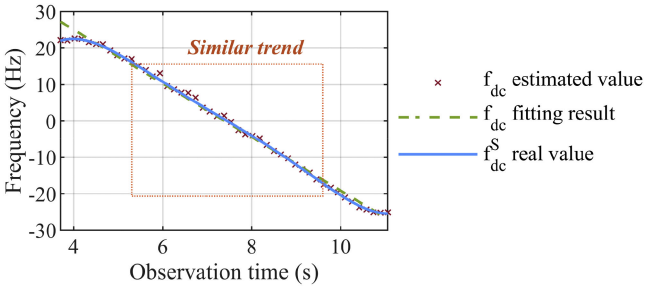

Fig. 9. Doppler frequency comparison between $\hat{f}_d(k)$ and $f_d^S(k)$ for the first target.

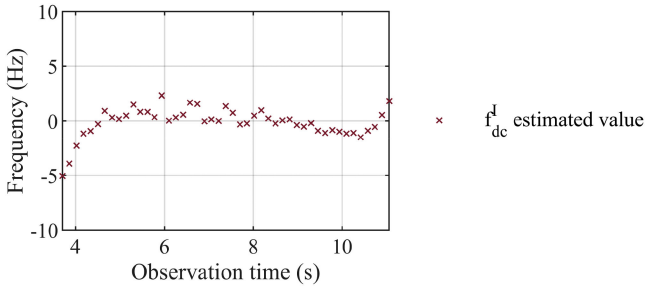

Fig. 10. Estimated values of residual Doppler frequency for the first target.

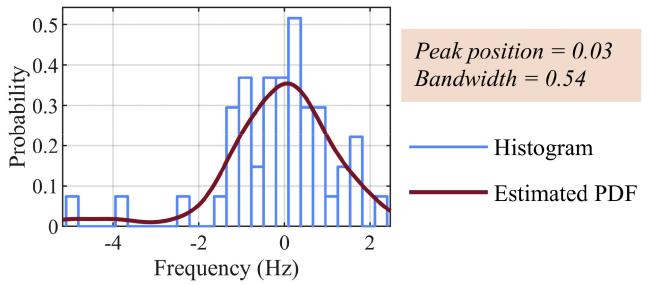

Fig. 11. Histogram and estimated PDF of $\hat{f}_d^I(k)$ for the first target.

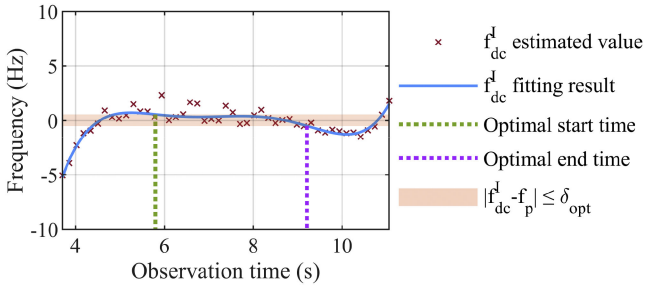

Fig. 12. Optimal imaging time interval of the first target.

and improve the image quality. The simulated results of two ship targets are shown as the following *Case 1* and *Case 2*, respectively.

Case 1. Imaging Results of Ship Target 1: After the extraction of range profile, the theoretical value of $f_d^S(k)$ can be obtained by (8), and the Doppler frequency center of echo can be estimated with the ACCC method in [29], both of which are shown in Fig. 9. Here, the red label "x," blue line and green dotted line in Fig. 9 represent the estimated value of $\hat{f}_d(k)$, fitting curve of $\hat{f}_d(k)$, and real value of $f_d^S(k)$, respectively. Obviously, the estimated values of $\hat{f}_d(k)$ and the real values of $f_d^S(k)$ have similar trends in the orange area.

Then, the residual Doppler frequency can be calculated via (15)–(17) as shown in Fig. 10. The stationarity of residual Doppler frequency is expressed as $|\hat{f}_d^I(k) - f_p| \leq \delta_{\text{opt}}$, through which the optimal processing time interval can be selected.

Afterwards, the PDF curve is estimated via the kernel distribution to determine f_p and δ_{opt}. The histogram and estimated PDF of $\hat{f}_d^I(k)$ are shown in Fig. 11, where the blue line and red line represent the histogram and estimated PDF, respectively. Obviously, the estimated values of $\hat{f}_d^I(k)$ are concentrated on $f_p = 0.03\,\text{Hz}$, and the optimal bandwidth via (35) is $\delta_{\text{opt}} = 0.54\,\text{Hz}$.

Based on f_p and δ_{opt}, the optimal time interval can be selected as shown in Fig. 12, where the red label "x," blue line, green and purple dotted line, and orange shadow area represent $\hat{f}_d^I(k)$, fitting curve of $\hat{f}_d^I(k)$, start and end imaging moment, and the area of $|\hat{f}_d^I(k) - f_p| \leq \delta_{\text{opt}}$, respectively.

The time interval and pulse number before and after the preprocessing are listed in Table III. Meanwhile, the theoretical complete illumination time interval and pulse number are given. Obviously, the time intervals after the preprocessing are

TABLE III
TIME INTERVALS AND PULSE OF THE FIRST TARGET NUMBER UNDER DIFFERENT CONDITIONS

Category	Time interval	Pulses
Before preprocessing	[3.6220 s, 11.1705 s]	1511
Complete illumination	[4.3780 s, 10.4145 s]	1208
After preprocessing	[5.8000 s, 9.2100 s]	683

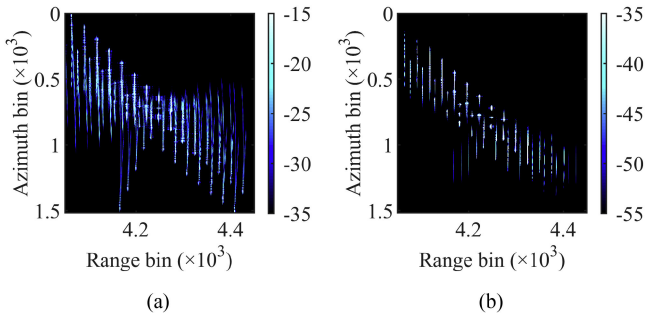

Fig. 13. Simulated data imaging results for the first target before preprocessing. (a) SAR image via CS algorithm. (b) Radar image via hybrid SAR and ISAR algorithm.

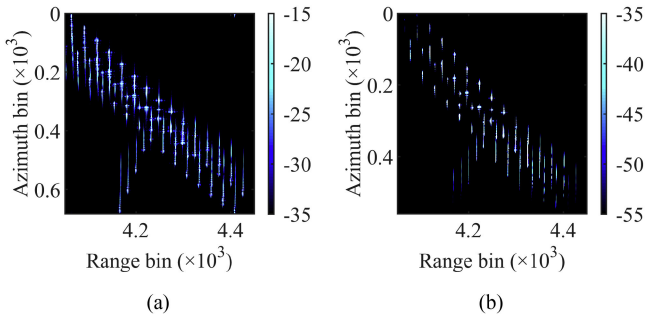

Fig. 14. Simulated data imaging results for the first target after preprocessing. (a) SAR image via CS algorithm. (b) Radar image via hybrid SAR and ISAR algorithm.

TABLE IV
ENTROPIES OF DIFFERENT RADAR IMAGES FOR THE FIRST TARGET

Preprocessing	Imaging algorithm	Image entropy
Before	CS algorithm	10.2056
	Hybrid SAR and ISAR algorithm	6.3330
After	CS algorithm	9.4326
	Hybrid SAR and ISAR algorithm	5.8924

within the complete illumination time interval. Compared with the result before the preprocessing, the pulse number after the preprocessing is decreased about 1.21 times. Since the size of processing data is decreased, the computational complexity can be degraded greatly.

The imaging results before and after the preprocessing for the first target are displayed in Figs. 13 and 14, where a) is the SAR image via the CS algorithm, and b) is the radar image via the hybrid SAR and ISAR algorithm. Compared with Fig. 13, the radar images in Fig. 14 have better quality. Especially, the SAR image in Fig. 13(a) has severe azimuth defocus, and the multiple imaging projection planes appear. After the SAR preprocessing, the quality of SAR image in Fig. 14(a) is improved obviously, and the imaging projection plane can be fixed. The improved quality is contributed by retaining the more stable Doppler frequency. The image entropies of Figs. 13 and 14 are listed in Table IV, from which we can see that the image entropies in Fig. 14 are lower.

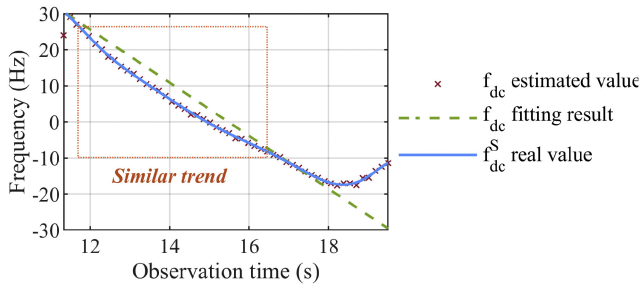

Fig. 15. Doppler frequency comparison between $\hat{f}_d(k)$ and $f_d^S(k)$ for the second target.

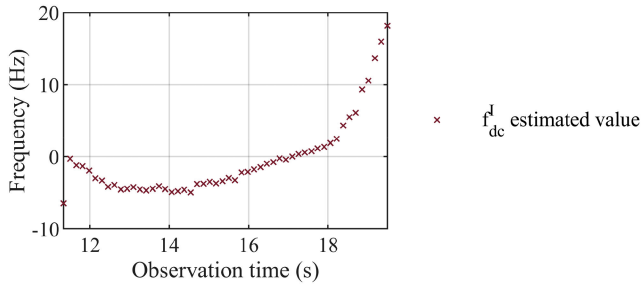

Fig. 16. Estimated values of residual Doppler frequency for the second target.

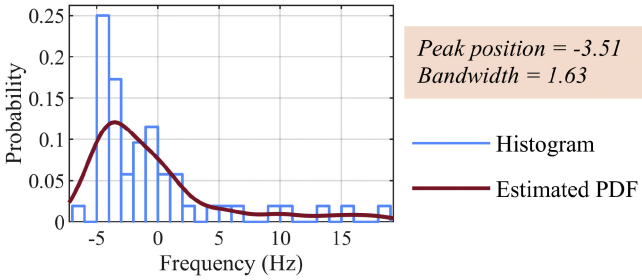

Fig. 17. Histogram and estimated PDF of $\hat{f}_d^I(k)$ for the second target.

Case 2. Imaging Results of Ship Target 2: First, the Doppler frequency comparison between $\hat{f}_d(k)$ and $f_d^S(k)$ is shown in Fig. 15. Obviously, the curves of $\hat{f}_d(k)$ and $f_d^S(k)$ have similar trends in the orange area of Fig. 15. Then, the estimated values of residual Doppler frequency are displayed in Fig. 16. With the kernel distribution, the histogram and estimated PDF curve are given in Fig. 17. After calculation, the central frequency is $f_p = -3.51\,\text{Hz}$ and the optimal bandwidth is $\delta_{\text{opt}} = 1.63\,\text{Hz}$. Afterward, the estimated values of $|\hat{f}_d^I(k) - f_p| \leq \delta_{\text{opt}}$ are utilized to obtain the optimal time interval as shown in Fig. 18.

In Table V, the time intervals and pulse number before and after the preprocessing are listed, and the time interval and pulse number of complete illumination time are given simultaneously. Obviously, the optimal time interval is totally within the complete illumination time, and the pulse number after the preprocessing is decreased about 1.01 times. Hence, the proposed approach can reduce the computational complexity for the hybrid SAR and ISAR imaging.

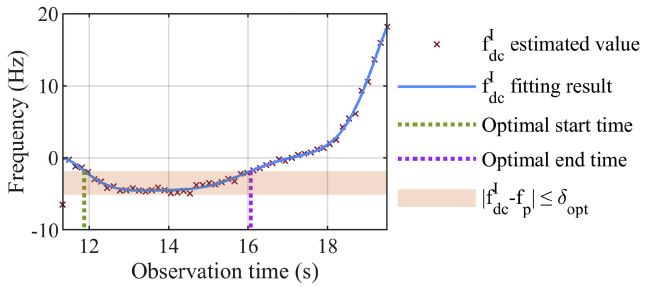

Fig. 18. Optimal imaging time interval of the second target.

TABLE V
TIME INTERVALS AND PULSE NUMBER OF THE SECOND TARGET UNDER DIFFERENT CONDITIONS

Imaging time	Time interval	Pulses
Before preprocessing	[11.2600 s, 19.7025 s]	1689
Complete illumination	[12.9100 s, 18.0525 s]	1029
After preprocessing	[11.8800 s, 16.0700 s]	839

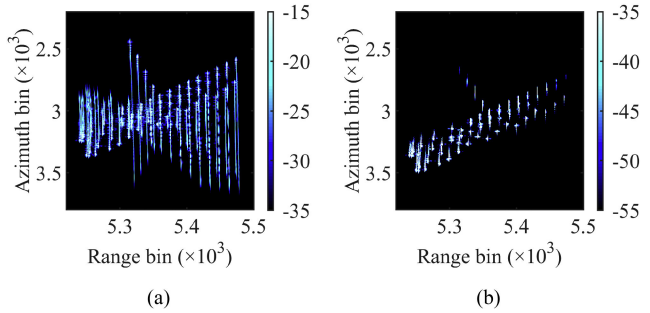

Fig. 19. Simulated data imaging results for the second target before preprocessing. (a) SAR image via CS algorithm. (b) Radar image via hybrid SAR and ISAR algorithm.

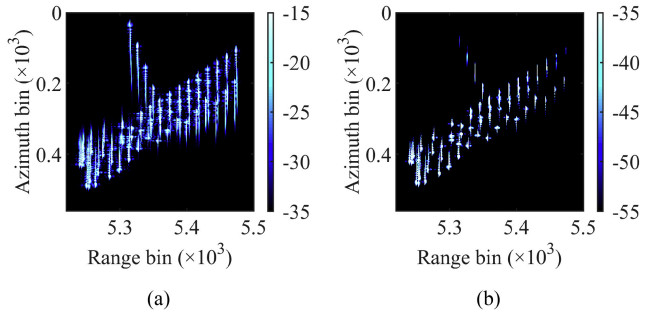

Fig. 20. Simulated data imaging results for the second target after preprocessing. (a) SAR image via CS algorithm. (b) Radar image via hybrid SAR and ISAR algorithm.

The hybrid SAR and ISAR imaging results before and after the preprocessing for the second target are shown in Figs. 19 and 20, where a) is the SAR image via the CS algorithm, and b) is the radar image via the hybrid SAR and ISAR algorithm. Clearly, there are two ship attitudes appear in Fig. 19(a) before the preprocessing, and only one ship attitude remains in Fig. 20(a) after the preprocessing. Hence, the proposed approach can enhance the performance of SAR imaging. Moreover, the image entropies in Figs. 19 and 20 are listed in Table VI, and the radar images in Fig. 20 have lower entropies.

TABLE VI
ENTROPIES OF DIFFERENT RADAR IMAGES FOR THE SECOND TARGET

Preprocessing	Imaging algorithm	Image entropy
Before	CS algorithm	10.2206
	Hybrid SAR and ISAR algorithm	6.7226
After	CS algorithm	9.4115
	Hybrid SAR and ISAR algorithm	6.7220

Given above, the proposed approach can reduce the computational complexity and ensure the image quality.

Remark 2: The use of SAR or ISAR imaging can be determined according to the specific cases. In the case of ship target with slight motion, the high-quality radar image can be obtained only with the SAR processing and the optimal time selection. In the case of ship target with maneuvering motion, the quality of SAR image can be improved obviously after the time selection, for example, the SAR image before the optimal time selection in Fig. 19(a) and the SAR image after the optimal time selection in Fig. 20(a). If the demand of the image quality is not strict, the ISAR refocusing technique does not have to be implemented. If the high-quality radar image is required, the ISAR refocusing technique needs to be implemented.

B. Comparison With the Existing Methods

In this article, the maximum contrast based automatic time window selection (MC-ATWS) technique in [22] is adopted for comparing with the proposed approach from the aspects of computational complexity and image quality.

The MC-ATWS technique can determine the optimal time interval by two steps as follows: first, the imaging central moment is located by the maximum image contrast of the image sequence; then, the time window length is gradually increased until the image contrast of the new image sequence stops increasing.

The proposed approach can select the optimal time interval by the residual Doppler frequency estimation and the PDF fitting with the kernel distribution. The peak position and bandwidth of kernel distribution reflect the stationarity of Doppler frequency, through which the optimal time interval is selected.

1) From the Aspect of Image Quality: As mentioned above, the MC-ATWS selects the optimal time interval by the maximum image contrast, which can guarantee the highest image quality. In this article, the proposed approach also considers the image quality and achieves it by selecting the stable Doppler frequency, while the highest image quality cannot be ensured.

2) From the Aspect of Computational Complexity: It is assumed that the MC-ATWS technique and the proposed approach can export the same optimal time interval, and the azimuth number is denoted as $N_a' = m_e - m_s + 1$.

In the MC-ATWS technique, first, the SAR algorithm and ISAR motion compensation technique need to process the echo data with the size of $N_a \times N_r$. Then, the ISAR imaging algorithm is implemented $(M + N)$ times for the echo data with

TABLE VII
COMPUTATIONAL COMPLEXITY OF THE PROPOSED APPROACH

Step	Computational complexity
Range compression of RD algorithm	$O\left[\left(3N_aN_r/2\right)\log_2^{N_r}+4N_aN_r\right]$
Doppler frequency center estimation	$O\left(4KN_{a0}N_r\right)$
PDF curve estimation	$O\left(4K^2\right)$

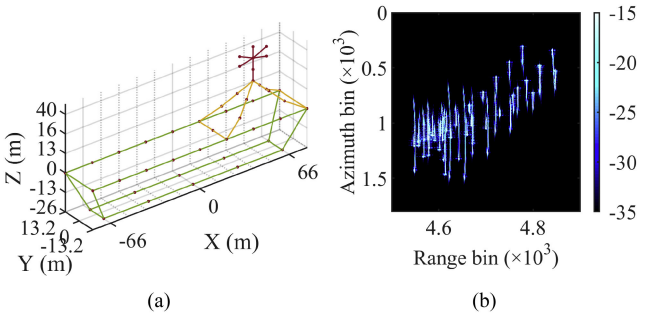

Fig. 21. Scatterer model and SAR imaging result. (a) Scatterer model. (b) SAR imaging result via CS algorithm.

TABLE VIII
TIME INTERVALS AND PULSE NUMBER UNDER DIFFERENT CONDITIONS

Imaging time	Time interval	Pulses
Before optimal time selection	[0.7460 s, 10.5463 s]	1961
Completely illumination	[3.7538 s, 7.5385 s]	758
MC-ATWS	[3.3000 s, 7.3000 s]	801
Processing via proposed approach	[3.8120 s, 7.5150 s]	741

the size about $N_a' \times N_r$ to select the optimal time interval. Hence, adopting the MC-ATWS technique requires the large computational complexity.

In the proposed approach, the computational complexity is mainly derived from the range compression for the echo data with the size of $N_a \times N_r$. After the optimal time interval selections, the SAR algorithm, ISAR motion compensation, and ISAR imaging algorithm are implemented one time for the echo data with the size of $N_a' \times N_r$. Therefore, the computational complexity can be smaller than the MC-ATWS technique. The computational complexity of the proposed approach is listed in Table VII. It is assumed that one time multiplication produces the computational complexity of $O(1)$.

Here, the simulation results are shown for the comparison of the MC-ATWS and the proposed approach. The parameters of radar system are same as Table I, and the ship target has the same motion parameters with the first target in Table II. The scatterer model and SAR image through the CS algorithm are shown in Fig. 21(a) and (b), respectively. Obviously, the azimuth defocus appears in Fig. 21(b) due to the target movement and long imaging time. Here, the MC-ATWS and the proposed approach are performed to determine the optimal time interval for reducing the computing time and enhancing the image quality.

The time interval and pulse number under the different conditions are listed in Table VIII. Without the time selection, the

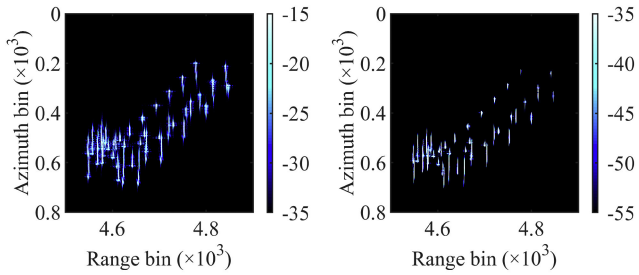

Fig. 22. Imaging results after optimal time selection through the MC-ATWS. (a) SAR image via CS algorithm. (b) Radar image via hybrid SAR and ISAR algorithm.

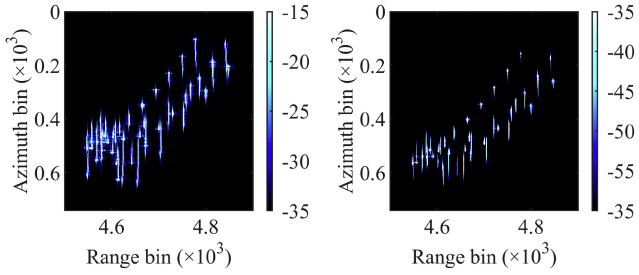

Fig. 23. Imaging results after preprocessing with the proposed approach. (a) SAR image via CS algorithm. (b) Radar image via hybrid SAR and ISAR algorithm.

TABLE IX
ENTROPIES OF DIFFERENT RADAR IMAGES

Methods	Imaging algorithm	Image entropy
MC-ATWS	CS algorithm	9.4558
	Hybrid SAR and ISAR algorithm	6.9431
Proposed approach	CS algorithm	9.4860
	Hybrid SAR and ISAR algorithm	7.0538

imaging time interval is [0.75 s, 10.55 s], and 1961 pulses need to be processed by the imaging algorithm. Actually, the target is completely illuminated in [3.75 s, 7.54 s], including 758 pulses.

Processing via the MC-ATWS technique, the time interval of [3.30 s, 7.30 s] is selected including 801 pulses. Although the MC-ATWS technique can decrease the computational complexity, the incomplete illumination time interval exists in [3.30 s, 7.30 s]. Hence, the processing pulse number can be smaller.

Processing via the proposed approach, the time interval of [3.81 s, 7.52 s] is chosen including 741 pulses, in which the target is completely illuminated. Hence, the proposed approach can reduce more computational complexity compared with the MC-ATWS technique.

Combining with the MC-ATWS technique, the radar images can be yielded via the CS algorithm and hybrid SAR and ISAR algorithm as shown in Fig. 22(a) and (b), respectively. Combining with the proposed approach, the radar images in Fig. 23(a) and (b) can be produced. The entropies of different radar images are listed in Table IX. Apparently, the radar image

TABLE X
PARAMETERS OF THE ACTUAL SAR DATA

Parameters	Values
Pulse width	10 μs
PRF	500 Hz
Carrier frequency	C band
Bandwidth	60 MHz
Range center	4.175 km
Aircraft velocity	50.9 m/s
Sampling frequency	100 MHz

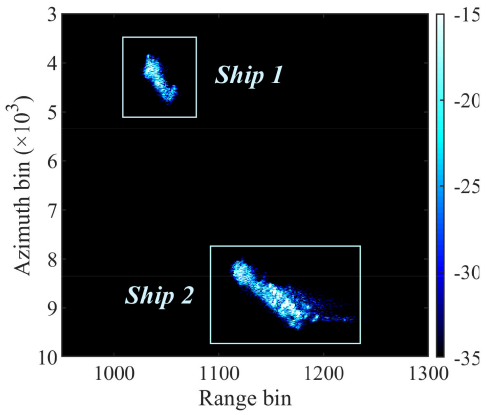

Fig. 24. SAR imaging result with CS algorithm.

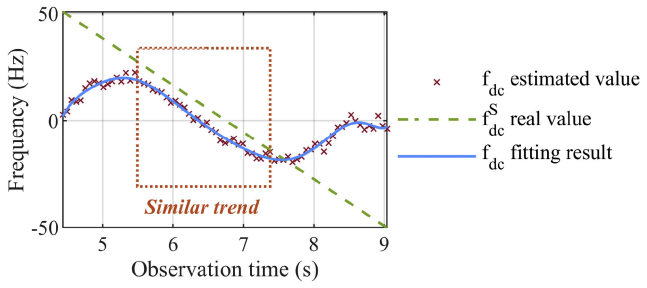

Fig. 25. Doppler frequency comparison between $\hat{f}_d(k)$ and $f_d^S(k)$ for the first target.

generated with the MC-ATWS technique has the better image quality.

C. Actual SAR Data

Afterwards, the results of actual SAR data are applied to verify the effectiveness of the proposed approach. The radar parameters are listed in Table X. The SAR image of the imaging scene is shown in Fig. 24, and the results of preprocessing and hybrid SAR and ISAR imaging are illustrated in the *Case 1* and *Case 2* as follows.

Case 1. Imaging Results of Ship Target 1: Firstly, the Doppler frequency comparison between $\hat{f}_d(k)$ and $f_d^S(k)$ is shown in Fig. 25, and the curves of $\hat{f}_d(k)$ and $f_d^S(k)$ have the similar trends in the orange area. There is a difference value between $\hat{f}_d(k)$ and $f_d^S(k)$ in the orange area, which is generated by the smooth movement of target, such as the translational motion

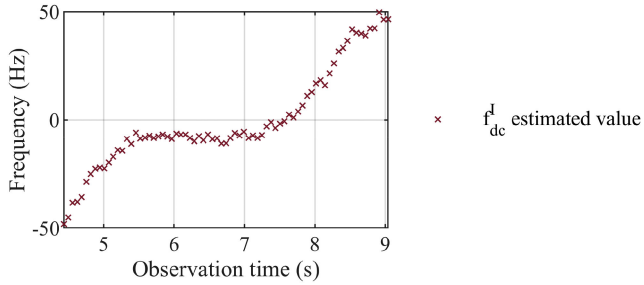

Fig. 26. Estimated values of residual Doppler frequency for the first target.

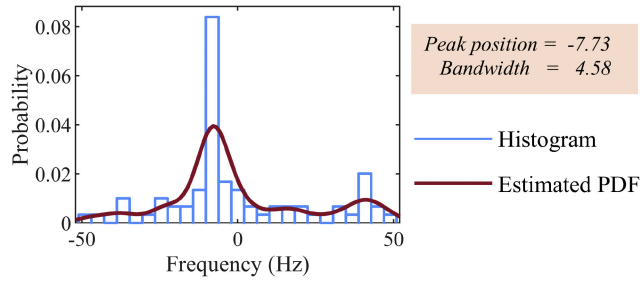

Fig. 27. Histogram and estimated PDF of $\hat{f}_d^I(k)$ for the first target.

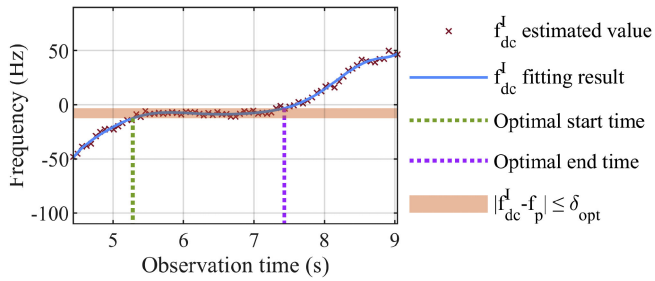

Fig. 28. Optimal imaging time interval of the first target.

and uniform rotational motion. The translational motion can be eliminated through the motion compensation technique, and the rotational motion can be used for the ISAR imaging. Hence, this difference will not affect the imaging quality. Moreover, this difference is denoted as f_p in fact, and will not influence the performance of the proposed approach because the Doppler frequency should satisfy the condition of $|\hat{f}_d^I(k) - f_p| \leq \delta_{\text{opt}}$.

Then, the residual Doppler frequency is estimated as shown in Fig. 26. For measuring the stationarity of residual Doppler frequency, the histogram and estimated PDF are yielded in Fig. 27. The optimal central frequency is determined as -7.73 Hz, and the optimal bandwidth is calculated as 4.58 Hz. Afterwards, the imaging time interval can be determined with $|\hat{f}_d^I(k) - f_p| \leq \delta_{\text{opt}}$, as shown in Fig. 28.

The time intervals and pulse numbers before and after the preprocessing are listed in Table XI, respectively. After the preprocessing, the processed pulse number is decreased about 1.18 times, which verifies that the proposed approach can reduce the computational complexity.

TABLE XI
TIME INTERVALS AND PULSE NUMBER FOR THE FIRST TARGET BEFORE AND AFTER PREPROCESSING

Imaging time	Time interval	Pulses
Before preprocessing	[4.40 s,9.10 s]	2351
After preprocessing	[5.28 s, 7.43 s]	1077

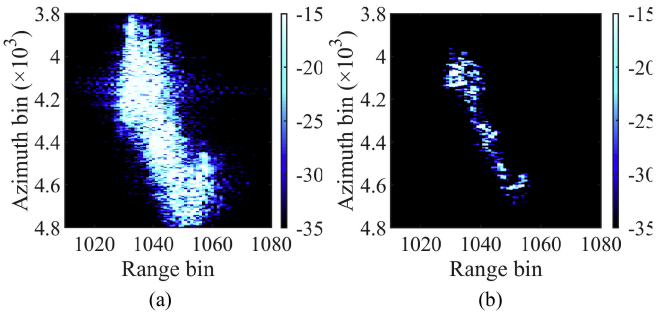

Fig. 29. Actual SAR data imaging results for the first target before the preprocessing. (a) SAR image via CS algorithm. (b) Radar image via hybrid SAR and ISAR algorithm.

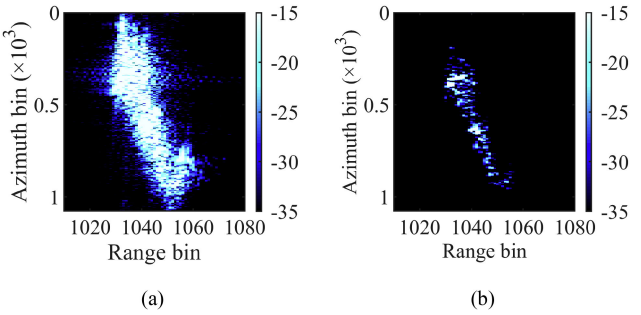

Fig. 30. Actual SAR data imaging results for the first target after the preprocessing. (a) SAR image via CS algorithm. (b) Radar image via hybrid SAR and ISAR algorithm.

TABLE XII
ENTROPIES OF DIFFERENT RADAR IMAGES FOR THE FIRST TARGET

Preprocessing	Imaging algorithm	Image entropy
Before	CS algorithm	8.9481
	Hybrid SAR and ISAR algorithm	6.2808
After	CS algorithm	8.8294
	Hybrid SAR and ISAR algorithm	6.1141

After the preprocessing, the hybrid SAR and ISAR imaging algorithm can be applied. The imaging results before and after the preprocessing for the first target are shown in Figs. 29 and 30, where a) is the SAR image via the CS algorithm, and b) is the radar image via the hybrid SAR and ISAR imaging algorithm. The image entropies of Figs. 29 and 30 are listed in Table XII, which describe that the radar images after the preprocessing have the equal quality with the radar images before the preprocessing.

Case 2. Imaging Results of Ship Target 2: First, the Doppler frequency comparison between $\hat{f}_d(k)$ and $f_d^S(k)$ is shown in Fig. 31. The orange area in Fig. 31 describes that the curves of $\hat{f}_d(k)$ and $f_d^S(k)$ have similar trends. Then, the residual Doppler

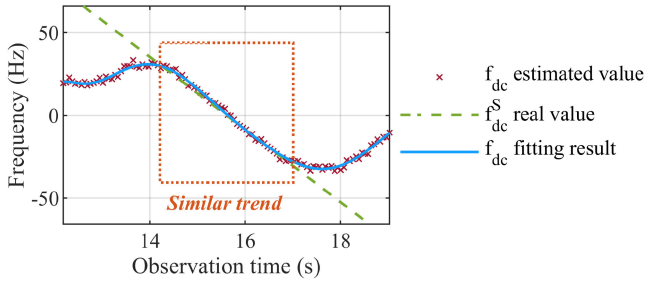

Fig. 31. Doppler frequency comparison between $\hat{f}_d(k)$ and $f_d^S(k)$ for the second target.

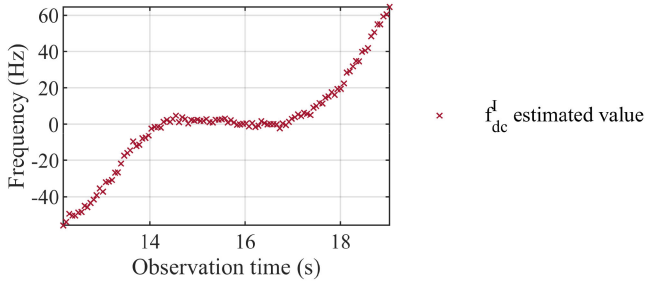

Fig. 32. Estimated values of residual Doppler frequency for the second target.

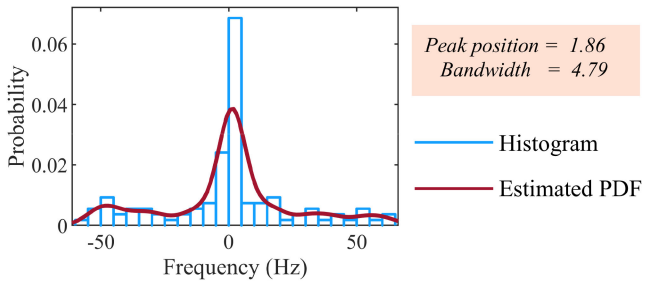

Fig. 33. Histogram and estimated PDF of $\hat{f}_d^I(k)$ for the second target.

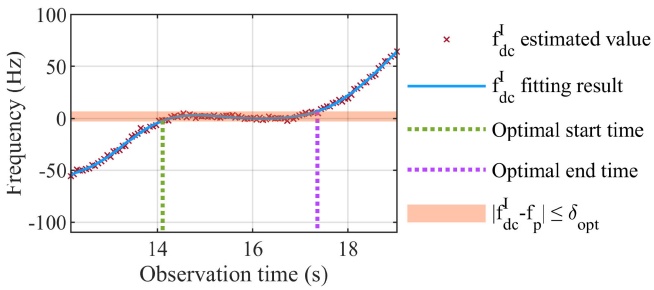

Fig. 34. Optimal imaging time interval of the second target.

frequency is estimated and shown in Fig. 32. To evaluate its stationarity, the PDF of $\hat{f}_d^I(k)$ is estimated as shown in Fig. 33, and the central frequency and optimal bandwidth is 1.86 and 4.79 Hz, respectively. Afterward, the optimal time interval can be selected as shown in Fig. 34.

The time intervals and pulse numbers before and after the preprocessing are listed in Table XIII, respectively. Compared with

TABLE XIII
TIME INTERVALS AND PULSE NUMBER OF THE SECOND TARGET BEFORE AND AFTER PREPROCESSING

Imaging time	Time interval	Pulses
Before preprocessing	[12.15 s, 19.06 s]	3458
After preprocessing	[14.11 s, 17.36 s]	1626

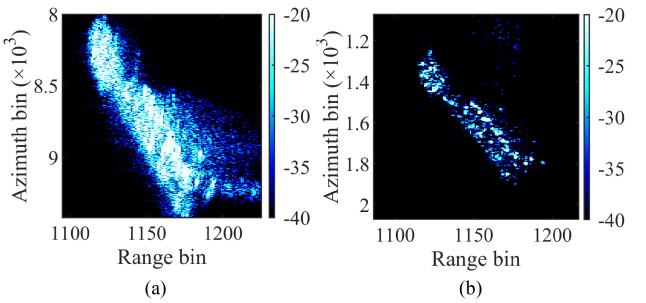

Fig. 35. Actual SAR data imaging results for the second target before the preprocessing. (a) SAR image via CS algorithm. (b) Radar image via hybrid SAR and ISAR algorithm.

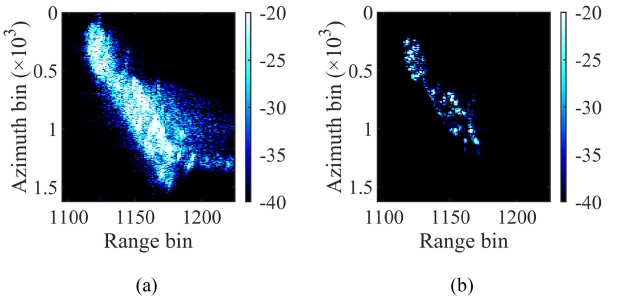

Fig. 36. Actual SAR data imaging results for the second target after the preprocessing. (a) SAR image via CS algorithm. (b) Radar image via hybrid SAR and ISAR algorithm.

TABLE XIV
ENTROPIES OF DIFFERENT RADAR IMAGES FOR THE SECOND TARGET

Preprocessing	Imaging algorithm	Image entropy
Before	CS algorithm	9.4740
	Hybrid SAR and ISAR algorithm	6.7523
After	CS algorithm	9.4360
	Hybrid SAR and ISAR algorithm	6.7474

the pulse number before the preprocessing, the pulse number is decreased about 1.13 times. Hence, the proposed approach can reduce the computational complexity.

The imaging results before and after the preprocessing for the second target are shown in Figs. 35 and 36, respectively, where a) is the SAR image via the CS algorithm, and b) is the radar image via the hybrid SAR and ISAR imaging algorithm. The image entropies are listed in Table XIV, which can illustrate that the image qualities before and after the preprocessing are equal.

Given above, the proposed approach can reduce the computational complexity and ensure the image quality.

V. CONCLUSION

In this article, an efficient preprocessing approach is proposed to address the issues of high computational complexity for the hybrid SAR and ISAR imaging procedure. The key of reducing computational complexity is to select the echo segment with the steady residual Doppler frequency after SAR processing.

First, the residual Doppler frequency is analyzed, which can reflect the status of illumination and movement of target. Then, the stationarity of the residual Doppler frequency is evaluated. Considering that the steady Doppler frequencies are concentrating on a stationary frequency, we applied the kernel distribution to determine the frequency range in which they locate. On this basis, the optimal imaging time interval can be selected, and the procedure of preprocessing approach can be accomplished.

The proposed approach can determine the optimal imaging time interval during the SAR processing, which can efficiently reduce the computational complexity and ensure the image quality. Radar imaging results of simulated and actual SAR data are given to illustrate the effectiveness of the novel method proposed in this article.

REFERENCES

[1] A. Sommer and J. Ostermann, "Backprojection subimage autofocus of moving ships for synthetic aperture radar," *IEEE Trans. Geosci. Remote Sens.*, vol. 57, no. 11, pp. 8383–8393, Nov. 2019.
[2] P. Liu and Y. Jin, "A study of ship rotation effects on SAR image," *IEEE Trans. Geosci. Remote Sens.*, vol. 55, no. 6, pp. 3132–3144, Jun. 2017.
[3] J. Wei, Y. Zhang, Y. Jiang, and X. Zhu, "A method of moving ship imaging and velocity estimation with airborne SAR," in *Proc. IEEE Int. Geosci. Remote Sens. Symp.*, 2021, pp. 4592–4595.
[4] Z. Li *et al.*, "Hybrid SAR-ISAR image formation via joint FrFT-WVD processing for BFSAR ship target high-resolution imaging," *IEEE Trans. Geosci. Remote Sens.*, vol. 60, 2022, Art. no. 5215713.
[5] A. Jain and I. Patel, "SAR/ISAR imaging of a nonuniformly rotating target," *IEEE Trans. Aerosp. Electron. Syst.*, vol. 28, no. 1, pp. 317–321, Jan. 1992.
[6] M. Martorella *et al.*, "ISAR based technique for refocusing noncooperative targets in SAR images," *IET Radar, Sonar Navigation*, vol. 6, no. 5, pp. 332–340, Jun. 2012.
[7] Y. C. Jiang and H. Y. Wang, "Hybrid SAR/ISAR imaging of ship targets based on parameter estimation," *Remote Sens. Lett.*, vol. 8, no. 7, pp. 657–666, 2017.
[8] J. B. Zheng, T. Su, G. S. Liao, H. Liu, Z. Liu, and Q. H. Liu, "ISAR imaging for fluctuating ships based on a fast bilinear parameter estimation algorithm," *IEEE J. Sel. Topics Appl. Earth Observ. Remote Sens.*, vol. 8, no. 8, pp. 3954–3966, Aug. 2015.
[9] J. B. Zheng, H. W. Liu, G. S. Liao, T. Su, Z. Liu, and Q. H. Liu, "ISAR imaging of nonuniformly rotating targets based on generalized decoupling technique," *IEEE J. Sel. Topics Appl. Earth Observ. Remote Sens.*, vol. 9, no. 1, pp. 520–532, Jan. 2016.
[10] R. Cao, Y. Wang, B. Zhao, and X. Lu, "Ship target imaging in airborne SAR system based on automatic image segmentation and ISAR technique," *IEEE J. Sel. Topics Appl. Earth Observ. Remote Sens.*, vol. 14, pp. 1985–2000, Jan. 2021.
[11] K. D. Ward and R. Tough, "High resolution radar imaging of the sea surface," in *Proc. IET Seminar High Resolution Imag. Target Classification*, 2006, pp. 39–52.
[12] K. D. Ward, R. J. A. Tough, and B. Haywood, "Hybrid SAR-ISAR imaging of ships," in *Proc. IEEE Int. Conf. Radar*, 1990, pp. 64–69.
[13] M. Martorella *et al.*, "ISAR based technique for refocusing non-cooperative targets in SAR images," *IET Radar Sonar Navigation*, vol. 6, no. 5, pp. 332–340, 2012.
[14] C. Noviello, G. Fornaro, and M. Martorella, "Focused SAR image formation of moving targets based on doppler parameter estimation," *IEEE Trans. Geosci. Remote Sens.*, vol. 53, no. 6, pp. 3460–3470, Jun. 2015.

[15] M. Martorella, D. Pastina, F. Berizzi, and P. Lombardo, "Spaceborne radar imaging of maritime moving targets with the Cosmo-skymed SAR system," *IEEE J. Sel. Topics Appl. Earth Observ. Remote Sens.*, vol. 7, no. 7, pp. 2797–2810, Jul. 2014.
[16] M. Martorella, F. Berizzi, E. Giusti, and A. Bacci, "Refocussing of moving targets in SAR images based on inversion mapping and ISAR processing," in *Proc. IEEE RadarCon*, 2011, pp. 068–072.
[17] F. Berizzi, G. Corsini, F. Gatri, and F. Gini, "Cumulant based algorithms for autofocusing in ISAR/SAR systems," in *Proc. 3rd IEEE Int. Conf. Image Process.*, 1996, pp. 887–890.
[18] X. Xu, F. Su, J. Gao, and X. Jin, "High-squint SAR imaging of maritime ship targets," *IEEE Trans. Geosci. Remote Sens.*, vol. 60, Dec. 2021, Art. no. 5200716.
[19] E. Casalini, J. Fagir, and D. Henke, "Moving target refocusing with the FMCW SAR system MIRANDA-35," *IEEE J. Sel. Topics Appl. Earth Observ. Remote Sens.*, vol. 14, pp. 1283–1291, Jan. 2021.
[20] P. Huang *et al.*, "High-resolution ISAR imaging for maneuvering targets based on iterative adaptive processing," *IEEE Trans. Comput. Imag.*, vol. 7, pp. 1093–1108, Oct. 2021.
[21] P. Huang, X.-G. Xia, M. Zhan, X. Liu, G. Liao, and X. Jiang, "ISAR imaging of a maneuvering target based on parameter estimation of multicomponent cubic phase signals," *IEEE Trans. Geosci. Remote Sens.*, vol. 60, Jan. 2022, Art. no. 5103918.
[22] M. Martorella and F. Berizzi, "Time windowing for highly focused ISAR image reconstruction," *IEEE Trans. Aerosp. Electron. Syst.*, vol. 41, no. 3, pp. 992–1007, Jul. 2005.
[23] N. Li, L. Wang, and D. Zhu, "Optimal ISAR imaging time selection of ship targets using real data," in *Proc. IET Int. Radar Conf.*, 2013, pp. 1–4.
[24] G. Li *et al.*, "A modified imaging interval selection method based on joint time-frequency analysis for ship ISAR imaging," in *Proc. EUSAR 12th Eur. Conf. Synthetic Aperture Radar*, 2018, pp. 1–6.
[25] P. Zhou *et al.*, "Time-frequency analysis-based time-windowing algorithm for the inverse synthetic aperture radar imaging of ships," *J. Appl. Remote Sens.*, vol. 12, no. 1, pp. 1–20, Jan. 2018.
[26] P. Zhou, X. Zhang, Y. Dai, W. Sun, and Y. Wan, "Time window selection algorithm for ISAR ship imaging based on instantaneous Doppler frequency estimations of multiple scatterers," *IEEE J. Sel. Topics Appl. Earth Observ. Remote Sens.*, vol. 12, no. 10, pp. 3799–3812, Oct. 2019.
[27] N. Li, Q. Shen, L. Wang, Q. Wang, Z. Guo, and J. Zhao, "Optimal time selection for ISAR imaging of ship targets based on time-frequency analysis of multiple scatterers," *IEEE Geosci. Remote Sens. Lett.*, vol. 19, Jan. 2022, Art. no. 4017505.
[28] X. L. Jia, H. J. Song, and W. J. He, "A novel method for refocusing moving ships in SAR images via ISAR technique," *Remote Sens.*, vol. 13, no. 14, 2021, Art. no. 2738.
[29] S. N. Madsen, "Estimating the Doppler centroid of SAR data," *IEEE Trans. Aerosp. Electron. Syst.*, vol. 25, no. 2, pp. 134–140, Mar. 1989.
[30] A. W. Bowman and A. Azzalini, *Applied Smoothing Techniques for Data Analysis*. New York, NY, USA: Oxford Univ. Press, 1997.
[31] R. K. Raney, H. Runge, R. Bamler, I. G. Cumming, and F. H. Wong, "Precision SAR processing using chirp scaling," *IEEE Trans. Geosci. Remote Sens.*, vol. 32, no. 4, pp. 786–799, Jul. 1994.
[32] A. Moreira, J. Mittermayer, and R. Scheiber, "Extended chirp scaling algorithm for air- and spaceborne SAR data processing in stripmap and ScanSAR imaging modes," *IEEE Trans. Geosci. Remote Sens.*, vol. 34, no. 5, pp. 1123–1136, Sep. 1996.
[33] D. Zhu, L. Wang, Y. Yu, Q. Tao, and Z. Zhu, "Robust ISAR range alignment via minimizing the entropy of the average range profile," *IEEE Geosci. Remote Sens. Lett.*, vol. 6, no. 2, pp. 204–208, Apr. 2009.
[34] X. H. Qiu, Y. Zhao, and S. Udpa, "Phase compensation for ISAR imaging combined with entropy principle," in *Proc. IEEE Antennas Propag. Soc. Int. Symp. Dig. Conjunction USNC/CNC/URSI North Amer. Radio Sci. Meeting*, 2003, pp. 195–198.
[35] P. Huang, H. Yang, Z. Zou, X.-G. Xia, and G. Liao, "Multichannel clutter modeling, analysis, and suppression for missile-borne radar systems," *IEEE Trans. Aerosp. Electron. Syst.*, early access, doi: 10.1109/TAES.2022.3147136.
[36] P. Huang, Z. Zou, X.-G. Xia, X. Liu, and G. Liao, "A novel dimension-reduced space-time adaptive processing algorithm for spaceborne multichannel surveillance radar systems based on spatial-temporal 2-D sliding window," *IEEE Trans. Geosci. Remote Sens.*, vol. 60, Mar. 2022, Art. no. 5109721.
[37] Z. C. Zhou *et al.*, "A new Doppler centroid estimation method for high-squint curved-trajectory airborne synthetic aperture radar," *Int. J. Remote Sens.*, vol. 40, no. 23, pp. 9003–9025, 2019.
[38] P. Hu, Y. Zhao, S. Xu, and Z. Chen, "Range instantaneous Doppler ISAR imaging based on combined spectrogram," in *Proc. IEEE Int. Conf. Signal Process., Commun. Comput.*, 2017, pp. 1–4.
[39] D. R. Wehner, *High Resolution Radar*, 2nd ed. Boston, MA, USA & London, U.K.: Artech House, 1995.
[40] Y. Wang, J. J. Gao, and Y. C. Jiang, *Ship Target Inverse Synthetic Aperture Radar Imaging and Recognition Technology*. Harbin, China: Harbin Institute of Technology Press, 2017.
[41] R. Cao, Y. Wang, C. Yeh, Y. Zhang, and X. Lu, "A novel optimal time window determination approach for ISAR imaging of ship targets," *IEEE J. Sel. Topics Appl. Earth Observ. Remote Sens.*, vol. 15, pp. 3475–3503, May 2022.

Rui Cao (Graduate Student Member, IEEE) was born in 1996. She received the B.S. degree in electronic information engineering from the Harbin Institute of Technology (HIT), Weihai, China, in 2018, and the M.S. degree in information and communication engineering from the HIT, Harbin, China, in 2020. She is currently working toward the Ph.D. degree in information and communication engineering with the HIT, Harbin, China.

Her research interests include the field of radar imaging and radar signal processing.

Yong Wang (Senior Member, IEEE) was born in 1979. He received the B.S. and M.S. degrees in electronic engineering from the Harbin Institute of Technology (HIT), Harbin, China, in 2002 and 2004, respectively, and the Ph.D. degree in information and communication engineering from the HIT, in 2008.

He is currently a Professor with the Institute of Electronic Engineering Technology, HIT. He has authored/coauthored more than 130 papers, most of them appeared in the journals of IEEE TRANS. GRS, *IET Signal Processing*, *Signal Processing*, etc. His research interests include time-frequency analysis of nonstationary signal, radar signal processing, and their application in synthetic aperture radar imaging.

Prof. Wang was the recipient of the Program for New Century Excellent Talents in University of Ministry of Education of China in 2012, and the Excellent Doctor's Degree nomination Award in China in 2010.

Yanchao Lin was born in Fujian, China, in 1989. He received the M.S. degree in information and communication engineering from the School of Electronics and Information Engineering, Harbin Institute of Technology, Harbin, China, in 2013.

He is currently an Engineer with the Beijing Aerospace Automatic Control Institute, Beijing, China. His research interests include radar signal and data processing.

Yun Zhang (Member, IEEE) was born in Heilongjiang, China, in November 1975. She received the B.S. and M.S. degrees in electronic engineering and the Ph.D. degree in information and communication engineering from the Harbin Institute of Technology (HIT), Harbin, China, in 2000, 2003, and 2009, respectively.

She is currently a Professor with the Research Institute of Electronic Engineering Technology, HIT. Her research interests include radar signal processing, synthetic aperture radar imaging, machine learning, and pattern analysis in remote sensing.